PAPER

Heterostructured Co₃O₄/PEI–CNTs composite: fabrication, characterization and CO gas sensors at room temperature†

Lifang Dang,[a] Guo Zhang,[a] Kan Kan,[ac] Yufei Lin,[a] Fuquan Bai,[d] Liqiang jing,[a] Peikang Shen,[e] Li Li*[ab] and Keying Shi*[a]

In this paper, a new controllable dispersion of Co₃O₄ nanoparticles (NPs) on multiwalled carbon nanotubes (CNTs) functionalized with branched polyethylenimine (PEI) is synthesized by a noncovalent method. In Co₃O₄/PEI–CNTs composite, CNTs not only prevent Co₃O₄ NPs from aggregation, but also provide an electron transfer path. The domain sizes of Co₃O₄ NPs on Co₃O₄/PEI–CNTs composite synthesized with hydrothermal time 5 h at 190 °C (named C-5) is about 4–8 nm. The surface area to volume ratio increases, the overlapped parts of Co₃O₄ grains contain high density of defects, which provides a greater number of available active centers for gas/surface reactions. The Co₃O₄/PEI–CNTs composite displays excellent sensitive characteristics to CO even at a level of 5 ppm at room temperature (RT). The C-5 sensor with rapid response property and excellent stability at RT shows highly promising applications in gas sensing.

1. Introduction

Carbon monoxide (CO) exposure may cause both acute and chronic health effects. But CO's pollution causing and harm to human health may be easily missed due to it being colorless and odorless. The Occupational Safety and Health Agency recommends a 10 h average exposure of 35 ppm, whereas the National Institute of Occupational Safety and Health recommends an 8 h average exposure of 50 ppm.[1] These demonstrate the importance of environmental gas sensing for continuous surveillance, to identify hazardous environment where significant CO levels exist. Thus, it is important to develop CO sensors and detect CO concentrations in factories, indoor atmosphere, vehicle emissions, natural gas emissions and industrial waste.

As an important p-type semiconductor, cobalt oxide (Co₃O₄) is of special interest due to its potential application as

[a]*Key Laboratory of Functional Inorganic Material Chemistry, Ministry of Education, Key Laboratory of Physical Chemistry, School of Chemistry and Material Science, Heilongjiang University, Harbin, 150080, P. R. China. E-mail: shikeying2008@163.com; llwjj@sohu.com; Fax: +86 4518667 3647; Tel: +86 451 8660 9141*

[b]*Key Laboratory of Chemical Engineering Process, Technology for High-efficiency Conversion, School of Chemistry and Material Science, Heilongjiang University, Harbin 150080, P. R. China*

[c]*Daqing Branch, Heilongjiang Academy of Sciences, Daqing 163319, P. R. China*

[d]*State Key Laboratory of Theoretical and Computational Chemistry, Institute of Theoretical Chemistry, Jilin University, Changchun 130023, China*

[e]*Department of Physics and Engineering, Sun Yat-sen University Guangzhou, 510275, P. R. China*

† Electronic supplementary information (ESI) available. See DOI: 10.1039/c3ta15019d

heterogeneous catalysts, magnetic properties, electrochromic devices and gas sensing.[2–4] Co₃O₄ with different morphologies such as nanoplates, well organised cabbage-like structures and microspherical composites was reported recently by Cao *et al.*[5] They investigated the CO and alcohol sensing properties of the synthesized nanostructured Co₃O₄. The synthesized nanostructured Co₃O₄ exhibited good sensitivity (>8–50 ppm) and response to alcohol at an operating temperature of 300 °C. It was found to be insensitive to 50 ppm CO at 300 °C but the resistance change was still at a much lower level for 1000 ppm CO.[6] Li *et al.*[7] prepared Co₃O₄ nanotubes by thermal decomposition of Co (NO₃)₂·6H₂O within ordered porous alumina templates and investigated the gas sensing characteristics of the nanotubes exposed to H₂ and alcohol. The prepared Co₃O₄ nanotubes exhibited excellent sensitivity to hydrogen and alcohol at room temperature. Sun *et al.* synthesized Co₃O₄ microspheres by the solvothermal method. The Co₃O₄ microspheres show much higher ethanol sensitivity and selectivity at a relatively low temperature (135 °C) as compared to those of commercial Co₃O₄ NPs.[8] Co₃O₄ semiconductor materials have good development prospects as gas sensors. However, it is difficult for a single oxide based semiconductor gas sensor to satisfy all practical requests: high and fast response, stability, and low energy consumption. To overcome these disadvantages, sensors based on two or more components have been explored for well-designed nanostructures and well-fabricated heterojunction interaction between these components.[9,10] Therefore, in recent years, much effort has been made to develop new methods for the preparation of Co₃O₄ composed nanomaterials, including thermal deposition and

hydrothermal synthesis *etc.*[11,12] These methods have emerged as attractive and simple routes for processing such metal oxide composite.

CNTs are promising building blocks for potential applications in many fields such as nanoelectronic and gas sensors due to their unique structure-dependent physical and chemical properties. CNTs have the potential to provide unique properties leading to advanced catalytic systems, and very sensitive photo/chemical sensors.[13–17] In particular, CNTs are ideal templates for the decoration of functional NPs. Surface functionalization and hybridization of CNTs currently attracts significant research interest.[18] So, CNTs were introduced into the gas sensitive materials to reduce the corresponding temperature.[19,20] Wu *et al.* doped 0.1% CNT into Co_3O_4–SnO_2 compositions. It was found that the sensor response varied under CO concentrations ranging from 20–1000 ppm at 25 °C. The response time was 21 s when the CO concentrations was 600 ppm. But the formation process of gas sensor compositions has not been further investigated.[21]

Herein, we present a simple noncovalent assembly of CNTs functionalized by PEI for density controllably and uniformly assembling the CNTs with Co_3O_4 nanoparticles (Co_3O_4/PEI–CNTs composite). This approach provided high density homogeneous functional groups on CNTs' sidewalls for binding Co^{2+} ions or/and Co_3O_4 NPs. The Co_3O_4 NPs are dispersed on conducting scaffold of PEI–CNTs. The beneficial aspects of the PEI–CNTs in improving the gas sensing performance of the Co_3O_4/PEI–CNTs composites are presented. The CNT-based hybrid composites are becoming the subject of increasing interest in exploiting large-area, low-cost, flexible electronic and gas sensing.

2. Experimental

2.1 Synthesis

All chemicals were purchased with analytical grade and used without further purification. CNTs are from Shenzhen Nanotech Port Co. Ltd, with a diameter of 30–80 nm and lengths ranging from 5–30 μm. The purity is higher than 99%. 2.4 mg CNTs functionalized by acid solution (HNO_3 : H_2SO_4 in 1 : 3 (v/v) ratio) and 4 mg PEI (branched PEI, M_W = 600, Aldrich) were dissolved and dispersed in 100 mL distilled water under magnetic stirring, the pH was adjusted to about 9.0 and kept for about 1 h. Then, 20 mL $Co(NO_3)_2$ solution of concentration about 2 mg mL^{-1} was added dropwise to the mixed solution. The pH was kept below 9.0 during the mixing process. Then, 90 mg mL^{-1} NaOH solution was slowly added to the solution, and the pH was adjusted to about 12.0. At the same time, the air flow was set to the solution with 50 mL min^{-1} for 2 h. Then, the mixed solution/precursor was placed for 24 h at RT. The precipitate was filtered and washed with deionized water. The obtained precipitate was dispersed in deionized water and transferred to a Teflon-lined stainless steel autoclave. Hydrothermal synthesis was conducted at 190 °C for 1, 3, 5 and 7 h, respectively. The obtained Co_3O_4/PEI–CNTs composites were named as C-1, C-3, C-5 and C-7 respectively.

2.2 Material characterizations

The structures and compositions of the as-prepared products were characterized by X-ray powder diffraction (XRD, D/max-III B-40 kV, Japan, Cu-Kα radiation, λ = 1.5406 Å). The structures of the synthesized samples were studied by TEM (JEOL-JEM-2100, 200 kV). The Fourier transform infrared (FT-IR) spectra were carried out with FT-IR Spectrometer (Perkin Elmer Spectrometer, KBr pellet technique). Thermogravimetric (TG-DTA) analysis of the samples was performed using a TA-SDTQ600. The air flow rate was maintained at 60 mL min^{-1}, and the temperature of the reactor was increased at a rate of 8 °C min^{-1}. Electrochemical impedance spectroscopy (EIS) and Mott–Schottky (MS) plot measurements were carried out using an electrochemical working station (CHI660C, Shanghai, China) in a half-cell setup configuration at rt. In EIS measurement the range of frequency was 0.01 Hz–100 kHz and the excitation amplitude was 5 mV.

2.3 Gas sensing tests

An alumina substrate (99.6% 7 × 5 × 0.38 mm) with two interdigitated Au electrodes on its top surface was used. Each Au electrode contained 100 fingers which interleaved each other, and the distance between two fingers was 20 μm (Fig. S1†). The Au electrodes were cleaned with diluted HCl, distilled water and acetone. A certain amount of Co_3O_4/PEI–CNTs composite was dispersed in ethanol to form a suspension. Sensors were fabricated by a simple drop-casting method and dried at 70 °C for 5 h. The sensor was installed into a test chamber with an inlet and outlet. The electrical resistance measurements of the sensor are carried out at rt and relative humidity (RH) around 26%. The CO gas concentration was controlled by injecting a volume of the gas and the chamber was purged with air to recover the sensor resistance. The sensor response[22] was defined as the ratio $(R_C - R_0)/R_0$%, where R_0 is the sensor resistance in air, and R_C is the resistance that in CO gas.

3. Results and discussion

3.1 Structure characterizations

Fig. 1 shows XRD patterns and FT-IR spectra of Co_3O_4/PEI–CNTs composite C-1, C-3, C-5 and C-7. Diffraction peaks around 19.0, 31.3 and 36.8° can be indexed as (111), (220) and (311) planes of face centered cubic phase of Co_3O_4.[23] The d spacings are 4.67, 2.86 and 2.44 Å, respectively, and the lattice parameters $a = b = c$ = 8.09 Å (JCPDS no. 78-1970). In addition, the XRD patterns of Fig. 1A exhibit two main well-resolved Bragg peaks of CNTs, corresponding to the 2θ of 26.2 and 41.4° (d spacing of 3.39, and 2.14 Å). These two main peaks can be indexed as (002) and (100) planes (JCPDS no. 75-1621). The width of the main peak of the CNTs at half-maximum height was obviously broadened, which indicates the walls of the CNTs were eroded during oxidation and the existence of defect sites.

Furthermore, the (220) and (311) peaks of C-5 and C-7 are obviously wider. The average crystallite size calculated from the XRD data is 8.83 nm. This implies that the existence of small
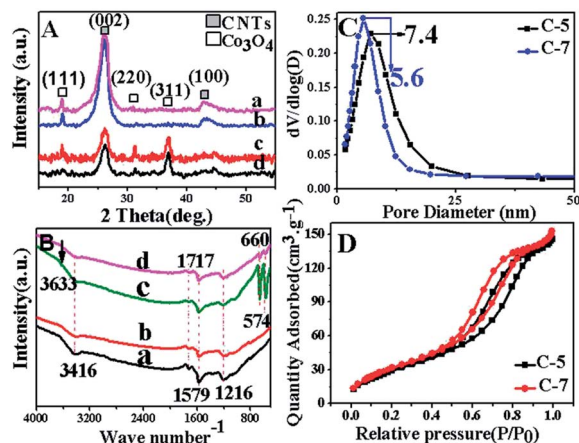
Fig. 1 (A) XRD diffraction patterns; (B) FT-IR spectra of Co_3O_4/PEI–CNTs composites synthesized by a hydrothermal method at 190 °C for different times (a) C-1, (b) C-3, (c) C-5 and (d) C-7; (C) the pore-size distribution curve and (D) N_2 adsorption–desorption isotherm of C-5 and C-7.

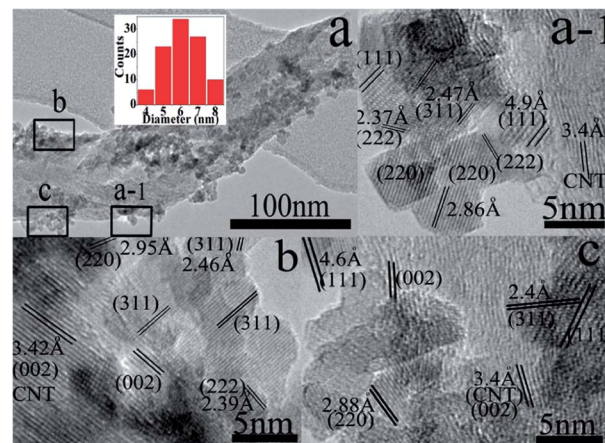**Fig. 2** TEM images of Co_3O_4/PEI–CNTs composite (C-5); (a) low magnification TEM image of C-5, inset shows the diameter distribution of (a); (a-1), (b) and (c) HRTEM images of (a).

Co_3O_4 NPs, when hydrothermal time was conducted at 190 °C for 5 or 7 h. There are no obvious (220) and (311) peaks existing in the C-1 and C-3. This indicates that Co_3O_4 crystalline phase of the Co_3O_4/PEI–CNTs composite can be controlled by changing the hydrothermal time. In addition, no obvious characteristic peaks of impurity phases (such as CoO and CoOOH) are present in the samples, indicating high purity of the final products.

The FT-IR spectra of the Co_3O_4/PEI–CNTs composites are shown in Fig. 1B. The broad peak dominating at about 3416 (3633) cm^{-1} corresponded to the N–H stretch of secondary amines and primary amines.[24] There are two weak absorption peaks at about 1579 and 1717 cm^{-1}, which is attributed to the carbonyl stretching vibration in –COOH groups.[25] In the region from 1100 to 1500 cm^{-1}, these absorption peaks correspond to several types of modes of PEI.[26] The sharp absorptions at 574 and 660 cm^{-1} correspond to Co(III)–O and Co(II)–O stretching vibrations of Co_3O_4.[27] From Fig. 1B, it can be seen that C-5 sample Co(III)–O and Co(II)–O stretching vibrations of Co_3O_4 is relatively stronger.

Fig. 1C and D shows the N_2 adsorption–desorption isotherms and BET pore size distribution plots of C-5 and C-7. The isotherm curve demonstrates type IV isotherms in the BET classification. The BET specific surface area and pore size of C-5 and C-7 are about 112, 96.9 $m^2 g^{-1}$ and 7.4, 5.6 nm respectively. The BET specific surface area and pore size of C-5 are larger than that of C-7.

The growth of Co_3O_4 nanocrystals on PEI–CNTs was confirmed by TEM and high-resolution transmission electron microscopy (HRTEM). The TEM/HRTEM images of C-1, C-3, C-5 and C-7 are shown in Fig. 2 and 3. Fig. 2a show that the Co_3O_4 NPs dispersed on the surface of PEI–CNTs and formed the composited structure. The sizes of Co_3O_4 NPs is about 4–8 nm. Fig. 2(a-1, b and c) is the HRTEM images of the C-5. The adjacent lattice fringes is around 4.6 (~4.9), 2.86 (~2.95), 2.4 (~2.47) and 2.37 (~2.39) Å, corresponding to the d spacing of the (111), (220), (311) and (222) planes of Co_3O_4, respectively. In addition,

the (002) plane of CNTs can be observed, and the lattice spacing of 3.4 (~3.42) Å was obtained. Moreover, Fig. 2b and c shows the defects at branching locations (interface) of Co_3O_4 NPs and CNTs, attributing to the linear and planar defects, which might be formed by the oxide defects caused by PEI.

Fig. 3(a, a-1), (b, b-1) and (c, c-1) are the TEM images of the C-1, C-3 and C-7 samples, respectively. The average distance between the adjacent lattice fringes is around 4.81, 2.91, 2.42 (~2.48), 2.01 (~2.04) and 1.82 (~1.84) Å, corresponding to the d spacing of the (111), (220), (311), (400) and (331) planes of
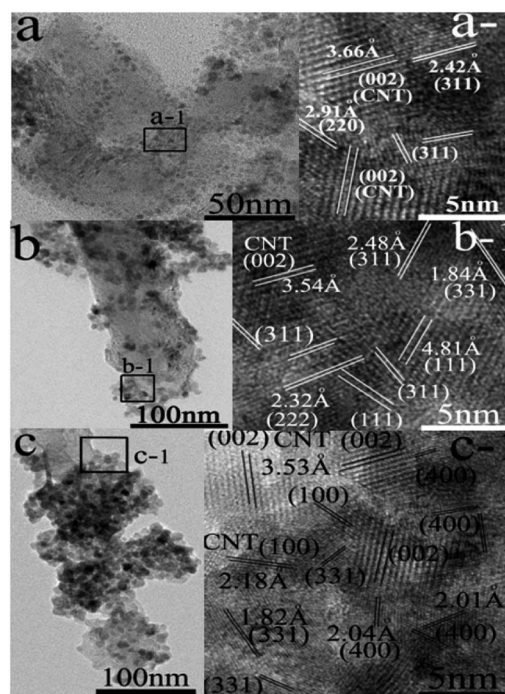

Fig. 3 TEM/HRTEM images of Co_3O_4/PEI–CNTs composites (a), (a-1) TEM/HRTEM images of the C-1; (b), (b-1) TEM/HRTEM images of the C-3; (c), (c-1) TEM/HRTEM image of the C-7.

Co_3O_4, respectively. Furthermore, the lattice fringes is 3.53 (~3.66) and 2.18 Å, corresponding to the *d* spacing of the (002) and (100) planes of CNTs. Fig. 3c appears to possess a loosely packed structure. The size of Co_3O_4 particles is 5–10 nm.

Similar to C-5, many defects existed in the samples between Co_3O_4 NPs and CNTs as shown in Fig. 3(a-1), (b-1) and (c-1). These have and irregular lattice, such as fringes with spacing of 2.42–2.48 Å corresponding to the (311) plane of Co_3O_4; spacing of 1.82–1.84 Å corresponding to the (331) plane and spacing of 2.01–2.04 Å corresponding to the (400) plane.

From all the above, it can be found that the Co_3O_4/PEI–CNTs composite materials with highly dispersed Co_3O_4 NPs on PEI–CNTs were prepared by a noncovalent method. The Co_3O_4 grains mostly anchor on defect and functionalization of CNTs or/and PEI–CNTs surface. The dispersion and particle size of Co_3O_4 on Co_3O_4/PEI–CNTs composite were controlled by changing the hydrothermal time. This could be confirmed by the results of TG-DTA and TEM.

Fig. 4 shows TG-DTA results of Co_3O_4/PEI–CNTs composites under N_2. As shown in Fig. 4a, there are two main exothermic peaks/oxidation peaks below 800 °C in C-1 and C-3, the temperatures of oxidation are 205 (206) and 349 (350) °C, respectively. The strongest peak at 349 (350) °C might be attributed to the oxidation peak of PEI. As for C-5 and C-7, the strongest peaks at 599 (or 607) °C might be attributed to the oxidation peak of CNTs due to the existence of Co_3O_4, which can be regarded as an oxygen reservoir under N_2. CNTs were oxidized using Co_3O_4 as the oxidant. Therefore, the exothermic/oxidation peaks between 500 and 800 °C are attributed to dissociation and oxidation of CNTs.[28]

The PEI content of the Co_3O_4/CNTs composites is calculated in the 200–400 °C temperature range. The calculated PEI content of the C-1, C-3, C-5 and C-7 samples is 10.7, 10.9, 8.02 and 6.39 mass%, respectively. For all samples, the synthesis conditions of PEI–CNTs are the same; hence, the PEI content of the five samples should also be the same. However, the results of TG are quite different. These indicate that the interaction of PEI with Co_3O_4 NPs increases with Co_3O_4 content and the hydrothermal time increasing. That is, in the assembling

process of the Co_3O_4/PEI–CNTs composite, the PEI might interact strongly with the CNTs *via* n–p stacking interaction, and providing a fixation point for Co_3O_4 NPs on the CNTs. The calculated Co_3O_4 content of the C-1, C-3, C-5 and C-7 samples is 6.98, 21.84, 45.1 and 32.5 mass% (see Table S1†) (the Co_3O_4 content of the C-190 synthesized by hydrothermal time for 4 h at 190 °C is 41.7 mass%, as described in our previous work[29]) respectively. For the C-1 and C-3 samples, the amount of Co_3O_4 is relatively lower. At the same time, accompanied with the Co_3O_4 amount of C-5 and C-7 samples increase, the oxidation peaks of CNTs widen and shift to a high temperature.

To study the electric characteristics of Co_3O_4/PEI–CNTs composite, MS and EIS measurements were carried out. Fig. 5 and S2† show MS plots of electrodes based on samples synthesized with different hydrothermal times. The negative slopes of MS plots of all samples show p-types semi-conducting behavior. The carrier density can be calculated from the slope of MS plots using eqn (1):

$$N_a = (-2/e_0\varepsilon\varepsilon_0)[d(1/C^2)/dV]^{-1} \qquad (1)$$

where e_0 is the fundamental charge constant, ε_0 is the permittivity of vacuum, ε is the relative permittivity of Co_3O_4 ($\varepsilon = 12.9$).[30] The carrier density of Co_3O_4 NPs, C-1, C-3, C-5 and C-7 were then calculated to be 3.50×10^{17}, 2.23×10^{17}, 1.33×10^{17}, 5.40×10^{17} and 2.30×10^{17} cm^{-3} at a frequency of 10 kHz, respectively. ε is the relative permittivity of CNTs ($\varepsilon = 10$).[31] The carrier density of CNTs and PEI–CNTs were 8.16×10^{18} and 1.96×10^{18} cm^{-3}. MS studies showed that the CNTs sample has a much higher carrier density than the PEI–CNTs sample. PEI is relatively stable n-type doping effect[32] and CNTs is p-type semiconductor, so the carrier density of PEI–CNTs is relatively low (Fig. S2(a and b)†). Similarly, the carrier density of the pure Co_3O_4 NPs (~3.50×10^{17}) is lower than that of the CNTs. Compared with other Co_3O_4/PEI–CNTs composite, the carrier density of C-5 is the biggest.

Generally, the particle size effects could positively influence catalytic activity and sensing performance. The sensing performance is particularly related to the space-charge layer (or Debye length), which can be calculated from eqn (2):

$$L_a = \sqrt{\left(\varepsilon\varepsilon_0 kT \left(N_a(e_0)^2\right)\right)^{-1}} \qquad (2)$$

where T is the experimental temperature, k is the Boltzmann constant ($k = 1.38 \times 10^{-23}$), N_a is the carrier density, and L_a is
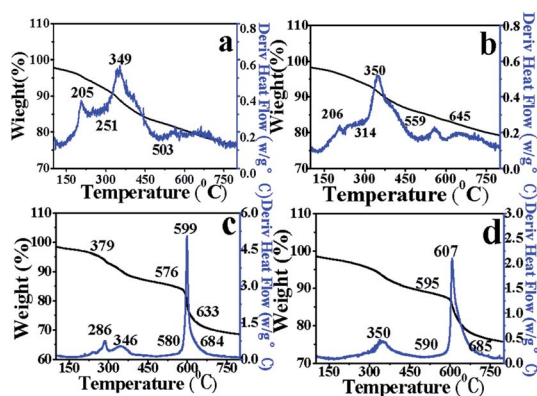

Fig. 4 TG-DTA curves of samples synthesized with different hydrothermal times with a temperature ramp of 8 °C min^{-1} under pure N_2 (a) C-1, (b) C-3, (c) C-5 and (d) C-7.
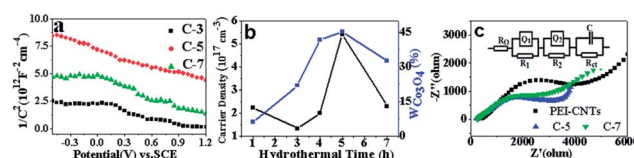

Fig. 5 (a) Mott–Schottky plots of sample (C-3, C-5 and C-7) electrodes in 3 M KOH solution with a frequency of 10 kHz; (b) relationship between the Co_3O_4 content, carrier density change and hydrothermal time and (c) Nyquist plots of different and equivalent circuit models of samples (inset) measured in the frequency range from 0.01 Hz to 100 kHz at 0.4 V.

This journal is © The Royal Society of Chemistry 2014

J. Mater. Chem. A, 2014, **2**, 4558–4565 | **4561**

the thickness of the space-charge layer (or Debye length). Here, if $N_a = 5.40 \times 10^{17}$, we estimated $L_a = 5.84$ nm.

Fig. 5b shows the relationship of the Co_3O_4 content, carrier density change and hydrothermal time. To the best of our knowledge, the resistance of materials in the air plays a key role in gas sensing responses. Better electron transportation in air induces a faster response. Thus, the electron transportation ability of the samples was studied, as shown in Fig. 5c and S2(c and d).†

To perform a quantitative analysis, an appropriate equivalent circuit,[33] as shown in Fig. 5c (inset) and S2,† is proposed to fit the impedance spectra, and the fitting results are listed in Table 1. For PEI–CNTs, C-5 and C-7 *etc.* the equivalent circuit used to fit the experimental data of the composite (Fig. 5c) consists of a resistance R_Ω in series with three subcircuits: higher frequencies (R_1Q_1), intermediate frequencies (R_2Q_2), and lower frequencies ($R_{ct}C$).

Here R_Ω refers to the resistance composed of solution resistance and electrode resistance Q_1 corresponding to the electrode film interface capacitance R_1 values have been related to Co_3O_4 grain boundaries in Co_3O_4/PEI–CNT scomposite,[33] subcircuit 2 is the response of CNTs. Subcircuit 3 is related to the response of amorphous carbon and impurities in the composite. R_{ct} is attributed to the charge-transfer resistance at the active material interface. C is the constant phase angle element, involving double layer capacitance.[33,34] Furthermore, the R_{ct} value of C-5 is 1686 Ω, which is the lowest among all samples (Table 1). C-5 exhibits much higher conductivity than the other samples. Therefore, C-5 can improve the electron transportation, which can be confirmed by the decreasing equivalent series resistance.

In addition, more detailed information on the chemical state of these elements is obtained from the high resolution XPS spectra of the O1s and Co2p peaks in Fig. 6 and S3.† For Co_3O_4/PEI–CNTs composites, the O_c peak at 530.0 eV is due to lattice oxygen of the Co_3O_4 the O_b peak at about 531.2 is generally attributed to oxide defect states[35] and the O_a peak at 532.7 eV are due to chemisorbed oxygen as shown in Fig. 6(a–c). The values of chemisorbed oxygen contents estimated from XPS measurements yielded 32.5, 35.2 and 29.1% for the C-1, C-5 and C-7. The calculated oxide defect of the three samples is about 35.2, 36.7 and 29.3%, respectively. The peak area of adsorbed oxygen and oxide defect on C-5 is bigger than the other samples.

In the Co2p range, the XPS spectra gives three main peaks (Fig. 6(d–f)) at 780.4 ± 0.3 eV, 781.8 ± 0.1 eV and 785.1 eV assigned to cobalt oxides (Co–O or Co–C),[36] Co–N[37] and Co salts.[38] The values of Co–N contents are about 39.3, 51.7, and 48.1% for C-1, C-5 and C-7, respectively, the calculated Co–O or Co–C of the three samples is about 27.9, 24.7 and 33.0%. The peak area of Co–N on C-5 is bigger than the other samples.
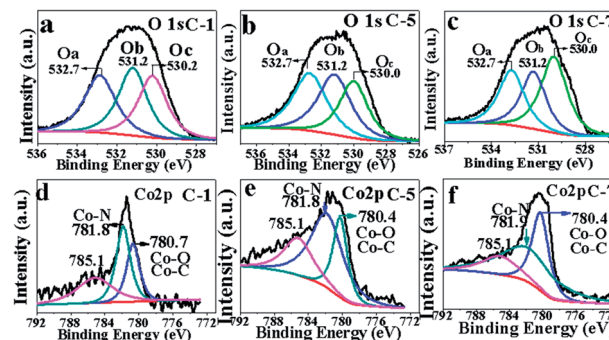

Fig. 6 XPS spectra of the O1s and Co 2p of (a), (d) C-1; (b), (e) C-5; (c), (f) C-7.

Therefore, the oxide defect on Co_3O_4/PEI–CNTs composite might be obtained and showed defects where Co–N (or Co–C) had existed. According to the Serge Palacin's studies, the Co–N structures and N-enriched carbon moieties are keys for high ORR activity.[36] Hence, Co–N structures and N-enriched carbon moieties are helpful for their good catalytic activity in gas sensing and improve the performance of CO sensors.

3.2 Sensing performance

The thin film sensor was fabricated by the Co_3O_4/PEI–CNTs composite. The CO gas sensing properties of the Co_3O_4/PEI–CNTs composite thin film sensor were investigated at RT.

Fig. 7a depicts representative dynamic gas responses of C-5 thin film sensor at CO concentrations ranging around 1000^{-5} ppm at rt. It can be seen that resistance undergoes a drastic rise upon injection of CO gas and a decline to its initial value after the sensors were exposed to air for some time to all samples. The comparison detail results of the response of C-1, C-3 and C-7 are shown in Fig. S4.† For 700 ppm CO, the gas response and response time of the C-5 thin film sensor are 27.4% and 8 s. When the concentration of CO is 500 and 300 ppm, the gas response and response time is 24.8, 23% and 4.7 and 4.7 s, respectively. That is faster than Co_3O_4–SnO_2–CNT,[21] whose response time is 21 s when the CO concentrations are 600 ppm; and also faster than C-190 sensors, as described in our previous work.[29] As can be seen in Fig. 7a, while the lowest detection limit of the thin film sensor is down to 5 ppm CO at RT, its response time is 43.3 s and the gas response is 3.2%. However without oxygen, the gas response of C-5 in pure nitrogen is very low (see Fig. S5†).

The thin film sensor fabricated based on a series of Co_3O_4/PEI–CNTs composites exhibit different degrees of response to CO in the detection range in Fig. 7b and c. As shown in Fig. 7a and b and S4,† except for C-4 (C-190),[29] the other sensors (C-1,

Table 1 Carrier density and fitted impedance parameters of the samples

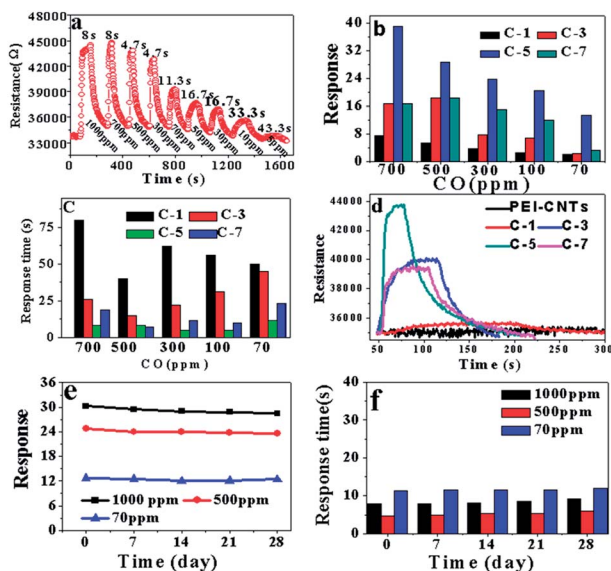| Samples	CNTs	PEI–CNTs	Co_3O_4	C-1	C-3	C-5	C-7
R_Ω (Ω)	207.9	428.6	1357	340.3	409.4	211.5	244.5
R_{ct} (Ω)	3317	4524	2923	6958	5564	1686	4352

Fig. 7 (a) Dynamic response–recovery curves of C-5 thin film sensor to CO at RT, (b) bar graphs represented the sensor response, (c) response time, (d) the response–recovery curve of the five sensors to 500 ppm CO at RT in air, (e) and (f) curves of the stability test of the gas response of for C-5 thin film sensor to 1000, 500 and 70 ppm CO at RT in air (HD: 26%).

C-3 and C-7) can not reach the lowest level (5 ppm). For the C-5, the response time to 1000 ppm CO is 8 s, the maximum response to 1000 ppm CO was 30.3%, which is the highest among all the sensors. In comparison with other samples, the thin film sensor based on C-5 exhibits a higher gas response, fast response/recovery time (see Table S2†) and lower detection limit than the other samples.

Fig. 7d shows typical response curves of the five sensors to CO (500 ppm) at rt in air for one circle. The response and response time of the C-1, C-3, C-5 and C-7 are 7.4, 11.9, 24.8, 18.3 and 40, 14.7, 4.7, 6.7 s respectively (the response of PEI–CNTs < 5%). The response of C-5 is the 3.4, 2.1 and 1.4 times of C-1, C-3 and C-7, respectively.

The stability of the C-5 thin film sensor is measured at different CO concentrations for 28 days. As shown in Fig. 7e and f, the response and response time to 1000, 500 and 70 ppm CO show little changes after 7 days. To activate the Co_3O_4/PEI–CNTs sensor (C-5) with 14 days aging, it was treated in a vacuum oven at 60 °C for 3 h. The response of the sensor was recovered, which conforms to the good stability of the C-5 sensor. Therefore, the mesoporous 1D structure of C-5 shows the potentials in sensor and related nanodevices.

3.3 Discussion of the sensing mechanism

From all the above, in Co_3O_4/PEI–CNTs composite, when CNTs architecture was employed as conducting scaffolds in Co_3O_4 semiconductor based sensor not only prevent Co_3O_4 nanoparticles from aggregation, but can also boost the electron transfer efficiency. PEI provided high density homogeneous functional groups on the CNTs' sidewalls for binding Co_3O_4 NPs. Meanwhile PEI is helpful for high density dispersion

Co_3O_4 grains, and enhances the interaction between Co_3O_4 grains and CNTs. Co_3O_4 NPs whose domain sizes of Co_3O_4 NPs on C-5 are between L_a (the thickness of the space-charge layer (or Debye length) of 5.84 nm) and $2L_a$ were dispersed on PEI–CNTs to improve the transport of the carriers to the surface.

The sensing mechanism of the Co_3O_4/PEI–CNTs composite to CO was analyzed based on its structure and composition. The discussion on the sensing mechanism consists of two points: (i) synergetic effect of gas sensing characteristic between one-dimensional (1D) Co_3O_4/PEI–CNTs composited structure and Co_3O_4 or PEI. (ii) The effects of the structure and composition of Co_3O_4/PEI–CNTs composite on the gas sensing performance such as Co_3O_4 NPs size, n–p or p–p heterostructure, carrier density, chemisorbed oxygen (O_2^-), defects etc.

In general, a high surface area provides an efficient space for gas adsorption sensing. C-5 possess a higher BET specific surface area of 112 m^2 g^{-1} and mesopores of 7.4 nm (Fig. 1), which is greatly advantageous for gas adsorption–desorption, diffusion and surface contact reaction. So, CO gas molecules diffused more easily inside the large mesopores 1D hollow composited structures of C-5. This can be in favour of the response to CO at rt.

For porous 1D nature of Co_3O_4/PEI–CNTs composite, the role of added CNT is a conducting wire and increases the electric conductivity of the sensing materials.[23,39] Therefore, the graphitized parts in CNTs offer a fluent electrical pathway,[40] resulting in fast migrating of electrons and response (see Scheme 1). As a result, C-5 sensor shows fast response to the CO concentrations ranging of 1000–5 ppm detection at rt.

The small size and appropriate electrical conductivity are crucial for improving the gas sensing performance of the materials. In our work, the domain size of Co_3O_4 NPs on C-5 is about 6 nm, which is between ($L_a = 5.84$ nm) and $2L_a$ (see Fig. 2 and 3). As Co_3O_4 NPs become smaller, the surface area to volume ratio increases, this would provide a greater number of available sites for gas/surface reactions to occur. Moreover, as
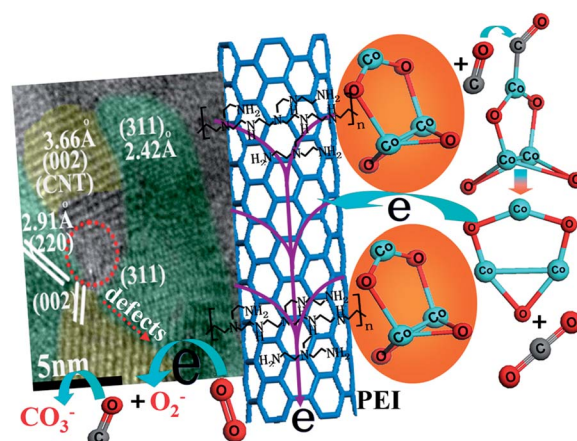
Scheme 1 Electronic transport characteristics and model of Co_3O_4/PEI–CNTs composite. On the left is a HRTEM image of Co_3O_4/PEI–CNTs composite, containing linear and planar defects, which might provide electrons to O_2 and occur R1–3; CO adsorbs on Co_3O_4 NPs and occur R4.

Co_3O_4 NPs size decreases, the interparticle connection sizes or "nanoparticle necks" become smaller and more numerous. The overlapped parts of Co_3O_4 grains contain a high density of defects. As a result, little Co_3O_4 NPs with a high density of defects form a large amount of sensing activity sites, which provides fast adsorption–desorption channels and accessibility of active centers for target gases.

Furthermore, Co_3O_4/PEI–CNTs composite, particularly C-5, the interaction of PEI with Co_3O_4 NPs enhances with Co_3O_4 content increasing. C-5 sample with the most dense attachment of the Co_3O_4 NPs (of 45.1 mass%) and carrier densities (of 5.40×10^{17}) has the lowest charge-transfer resistance R_{ct} of 1686 Ω among all the samples. These can make electrons transport easily, and allow carriers to diffuse freely. This benefits gas detection.
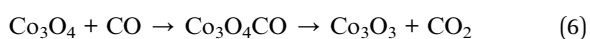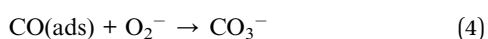
In the Co_3O_4/PEI–CNTs composite, the PEI–CNTs contained chemisorbed oxygen. Co_3O_4 NPs contained oxide defect states and also chemisorbed oxygen. These are suggested to act as an electron donor or shallow energy level. This demonstrates that a n–p heterostructure might be formed between the interface of the PEI and CNTs or PEI and Co_3O_4. The oxide defects caused impurity bands in the bandgap of CNTs or Co_3O_4. Meanwhile, p–p homotype heterostructure might be formed at the interface of Co_3O_4 and CNTs. Also, the defects between CNTs and Co_3O_4 NPs cause impurity bands in the bandgap of Co_3O_4/PEI–CNTs. There are a lot of Co–N or Co–C, chemisorbed oxygen and oxygen defects existing in n–p or p–p heterostructure of Co_3O_4/PEI–CNTs composite.

The model is introduced to explain the sensing mechanism in Scheme 1. The electronic transport and the CO gas response in the C-5 are as follows.

Firstly, the sensor is exposed to air. Then, oxygen molecules tend to trap and react with the electrons from Co_3O_4/PEI–CNTs composite conduction band. The produced negative oxygen species (O_2^-) causes the depletion layer (see the reaction 1 (R1)).

Secondly, when the sensor film is exposed to reducing gas CO, the CO molecules react with O_2^- to form CO_3^- (R2). Then CO_3^- molecules react with CO to form CO_2 (R3). At this stage, the electrons are released back to the Co_3O_4/PEI–CNTs composite which leads to the thickness of space-charge layer becoming thinner. This process decreases holes density and rapid increasing of the resistance (Fig. 7a).

Thirdly, CO molecule is favorable for adsorbing on the Co^{3+} ions in the octahedral coordination of the Co_3O_4. The oxidation of adsorbed CO occurs by abstracting the surface oxygen that might be coordinated with three Co^{3+} cations.[41] The electron transfer from adsorbates CO to the Co^{3+} of Co_3O_4 NPs, and the CO molecules are activated and formed CO_2 (R4).[42]

$$O_2 + e^- \rightarrow O_2^- \qquad (3)$$

$$CO(ads) + O_2^- \rightarrow CO_3^- \qquad (4)$$

$$CO_3^- + CO(ads) \rightarrow 2CO_2 + e^- \qquad (5)$$

$$Co_3O_4 + CO \rightarrow Co_3O_4CO \rightarrow Co_3O_3 + CO_2 \qquad (6)$$

Finally, the partially reduced cobalt site, which might be a Co^{2+} cation, is re-oxidized by a gas-phase neighbouring oxygen molecule to be an active Co^{3+} site.

4. Conclusion

A simple and efficient noncovalent chemical approach is developed for elaborately hybridizing the PEI–CNTs with the Co_3O_4 nanoparticles. The as-prepared Co_3O_4/PEI–CNTs composite synthesized by hydrothermal method at 190 °C for 5 h. The sensor exhibits excellent sensing properties at rt to CO detection: when the concentration of CO is 1000 ppm, the gas response is 39%, the response time is only 8 s, and the detection limit of the sensor is down to 5 ppm CO at RT.

The enhanced gas sensing could be ascribed to the synergistic effects of the mesopores 1D composited structures attached by 4–8 nm Co_3O_4 nanoparticles and the role of the PEI on the sensor characteristics. The unique 1D structure of Co_3O_4/PEI–CNTs with a high surface-to-volume ratio can act as channels for gas adsorption–desorption and diffusion. That provides more approachable active sites for the reaction of CO with surface-adsorbed oxygen ions, which resulted in a favorable response to CO at room temperature. Also, Co_3O_4 to PEI–CNTs might significantly increase the carrier densities, chemisorbed oxygen and defects; the PEI might enhance the interaction between CNTs and Co_3O_4 NPs, thus allowing carriers to diffuse freely, which benefits improving the performance of CO sensors.

The assembly method can be easily adapted to controllably produce various nanoparticles and PEI–CNT hybrid materials. This facile approach represents a potential and simple chemical route to control nanoparticles density and dispersity to form heterogeneous nanostructures on CNTs by utilizing PEI noncovalent assembly.

Acknowledgements

References

1 B. L. Risavi, R. J. Wadas Jr, C. Thomas and D. F. Kupas, J. Emerg. Med., 2013, **44**, 637–640.

2 L. Hu, Q. Peng and Y. Li, J. Am. Chem. Soc., 2008, **130**, 16136–16137.

3 L. Hu, Q. Peng and Y. Li, ChemCatChem, 2011, **3**, 868–874.

4 Y. Sun, P. Lv, J.-Y. Yang, L. He, J.-C. Nie, X. Liu and Y. Li, Chem. Commun., 2011, **47**, 11279–11281.

5 A.-M. Cao, J.-S. Hu, H.-P. Liang, W.-G. Song, L.-J. Wan, X.-L. He, X.-G. Gao and S.-H. Xia, J. Phys. Chem. B, 2006, **110**, 15858–15863.

6 D. Patil, P. Patil, V. Subramanian, P. A. Joy and H. S. Potdar, *Talanta*, 2010, **81**, 37–43.

7 W.-Y. Li, L.-N. Xu and J. Chen, *Adv. Funct. Mater.*, 2005, **15**, 851–857.

8 C. Sun, S. Rajasekhara, Y. Chen and J. B. Goodenough, *Chem. Commun.*, 2011, **47**, 12852–12854.

9 C. Zhao, G. Zhang, W. Han, J. Fu, Y. He, Z. Zhang and E. Xie, *CrystEngComm*, 2013, **15**, 6491–6497.

10 H. Yang, S. Wang and Y. Yang, *CrystEngComm*, 2012, **14**, 1135–1142.

11 J. R. Sietsma, J. D. Meeldijk, J. P. den Breejen, M. Versluijs-Helder, A. J. van Dillen, P. E. de Jongh and K. P. de Jong, *Angew. Chem.*, 2007, **119**, 4631–4633.

12 S. K. Meher and G. R. Rao, *J. Phys. Chem. C*, 2011, **115**, 15646–15654.

13 Z. Wen, Q. Wang, Q. Zhang and J. Li, *Adv. Funct. Mater.*, 2007, **17**, 2772–2778.

14 G. G. Wildgoose, C. E. Banks and R. G. Compton, *Small*, 2006, **2**, 182–193.

15 V. Georgakilas, D. Gournis, V. Tzitzios, L. Pasquato, D. M. Guldi and M. Prato, *J. Mater. Chem.*, 2007, **17**, 2679–2694.

16 B. Wu, D. Hu, Y. Kuang, B. Liu, X. Zhang and J. Chen, *Angew. Chem., Int. Ed.*, 2009, **48**, 4751–4754.

17 S. Liu, J. Li, Q. Shen, Y. Cao, X. Guo, G. Zhang, C. Feng, J. Zhang, Z. Liu and M. L. Steigerwald, *Angew. Chem.*, 2009, **121**, 4853–4856.

18 Z. Tan, H. Abe, M. Naito and S. Ohara, *Chem. Commun.*, 2010, **46**, 4363–4365.

19 W. Li, H. Jung, N. D. Hoa, D. Kim, S.-K. Hong and H. Kim, *Sens. Actuators, B*, 2010, **150**, 160–166.

20 J. Yang, W.-d. Zhang and S. Gunasekaran, *Electrochim. Acta*, 2011, **56**, 5538–5544.

21 R.-J. Wu, J.-G. Wu, M.-R. Yu, T.-K. Tsai and C.-T. Yeh, *Sens. Actuators, B*, 2008, **131**, 306–312.

22 A. D'Amico and C. Di Natale, *IEEE Sens. J.*, 2001, **1**, 183–190.

23 S. K. Meher and G. R. Rao, *J. Phys. Chem. C*, 2011, **115**, 25543–25556.

24 N. M. Rocher and R. Frech, *Macromolecules*, 2005, **38**, 10561–10565.

25 K. Kan, T. Xia, L. Li, H. Bi, H. Fu and K. Shi, *Nanotechnology*, 2009, **20**, 185502.

26 S. S. York, S. E. Boesch, R. A. Wheeler and R. Frech, *Macromolecules*, 2003, **36**, 7348–7351.

27 C. Nethravathi, S. Sen, N. Ravishankar, M. Rajamathi, C. Pietzonka and B. Harbrecht, *J. Phys. Chem. B*, 2005, **109**, 11468–11472.

28 W. Yan, J. Tang, Z. Bian, J. Hu and H. Liu, *Ind. Eng. Chem. Res.*, 2012, **51**, 3653–3662.

29 G. Zhang, L. Dang, L. Li, R. Wang, H. Fu and K. Shi, *CrystEngComm*, 2013, **15**, 4730–4738.

30 S. Thota, A. Kumar and J. Kumar, *Mater. Sci. Eng., B*, 2009, **164**, 30–37.

31 W. Lu, D. Wang and L. Chen, *Nano Lett.*, 2007, **7**, 2729–2733.

32 S. M. Kim, J. H. Jang, K. K. Kim, H. K. Park, J. J. Bae, W. J. Yu, I. H. Lee, G. Kim, D. D. Loc and U. J. Kim, *J. Am. Chem. Soc.*, 2008, **131**, 327–331.

33 D. Cai, P. Lian, X. Zhu, S. Liang, W. Yang and H. Wang, *Electrochim. Acta*, 2012, **74**, 65–72.

34 Q. Wang, D. Wang and B. Wang, *Int. J. Electrochem. Sci.*, 2012, **7**, 8753–8760.

35 S. C. Petitto, E. M. Marsh, G. A. Carson and M. A. Langell, *J. Mol. Catal. A: Chem.*, 2008, **281**, 49–58.

36 A. Morozan, P. Jégou, B. Jousselme and S. Palacin, *Phys. Chem. Chem. Phys.*, 2011, **13**, 21600–21607.

37 K. Niu, B. Yang, J. Cui, J. Jin, X. Fu, Q. Zhao and J. Zhang, *J. Power Sources*, 2013, **243**, 65–71.

38 K. Artyushkova, S. Levendosky, P. Atanassov and J. Fulghum, *Top. Catal.*, 2007, **46**, 263–275.

39 W.-D. Zhang, B. Xu and L.-C. Jiang, *J. Mater. Chem.*, 2010, **20**, 6383–6391.

40 Y. Wang, H. J. Zhang, L. Lu, L. P. Stubbs, C. C. Wong and J. Lin, *ACS Nano*, 2010, **4**, 4753–4761.

41 B. Mehrabi Matin, Y. Mortazavi, A. A. Khodadadi, A. Abbasi and A. Anaraki Firooz, *Sens. Actuators, B*, 2010, **151**, 140–145.

42 Y. Xie, F. Dong, S. Heinbuch, J. J. Rocca and E. R. Bernstein, *Phys. Chem. Chem. Phys.*, 2010, **12**, 947–959.